22

Structure and Dynamics of Model Membrane Systems Probed by Elastic and Inelastic Neutron Scattering

T. Salditt, M.C. Rheinstädter

22.1 Introduction

Phospholipid membranes are intensively studied as simple model systems to understand fundamental structural and physical aspects of their much more complex biological counterparts [1]. The lateral structure of membranes, including both height and compositional fluctuations, remains an important experimental challenge of present-day biophysics, concerning in particular the biologically relevant fluid L_α state, where the material softness compromises the use of scanning probe microscopy. Neutron scattering can contribute to the elucidation of the molecular structure, as is well documented in the literature (see, e.g., [2]).

Dynamical properties are often less well understood in biomolecular systems, but are important for many fundamental biomaterial properties, e.g., elasticity properties and interaction forces. Furthermore, lipid membrane dynamics on small molecular length scales determines or strongly affects functional aspects, like diffusion and parallel or perpendicular transport through a bilayer. The specific advantages of neutron scattering to study fluctuations of phospholipid membranes on lateral length scales between several micrometer down to a few Ångströms can give unique insights.

The present chapter concentrates on mainly two neutron scattering techniques, which give information on very different types of dynamics: (i) nonspecular neutron reflectivity (NSNR) as a tool to probe thermal fluctuations of lipid bilayers on mesoscopic length scales, and (ii) inelastic neutron scattering (INS) for studies of the short-range collective motions in the acyl chains. The methods can also be applied to more complex model systems, including lipid – peptide and lipid–protein mixtures, as well as in some cases to real biological membranes like purple membranes.

The chapter is so organized that at first sample preparation and sample environment for multilamellar lipid phases on solid support is presented. Next, specular neutron reflectivity (SNR) and NSNR from lipid membranes is described. Mainly work on pure lipid phases is presented and reviewed, a

few examples relate to structure and interaction of the antimicrobial peptide Magainin 2 in phosphocholine bilayers, as an example of how the methods presented can be extended and applied to probe lipid – peptide interaction or more generally the interaction of bilayers with membrane-active molecules (such as stereols, peptides, and proteins). Afterward recent advances are highlighted in the application of classical INS at triple-axis spectrometers (TAS) to study the short-range dynamics of lipid bilayers, e.g., the collective motion of the acyl chains. The chapter closes with a summary and conclusions.

22.2 Sample Preparation and Sample Environment

Highly oriented multilamellar bilayers for neutron reflectivity can be easily prepared on cleaned silicon wafers ((1 1 1)-orientation or (1 0 0)-orientation) by spreading from organic solution [3]. The wafers are cleaned by subsequent washing in methanol and ultrapure water (specific resistivity $\geq 18\,\mathrm{M\Omega\,cm}$), and made hydrophilic by washing in a 5-molar solution of KOH in ethanol for about a minute, or alternatively by plasma etching. Lipid and/or peptide components are codissolved in the desired ratio (molar ratio P/L) in trifluoroethanol (TFE) or (1:1) TFE–chloroform mixtures at concentrations between 10 and $40\,\mathrm{mg\,ml^{-1}}$, depending on the total mass to be deposited.

After a slow evaporation process avoiding film rupture, remaining traces of solvent in the sample are removed by exposing the samples to high vacuum overnight. Then the films are rehydrated in a hydration chamber and tempered above the main phase transition. The orientational alignment of such multilamellar stack with respect to the substrate (mosaicity) is typically better than 0.01°. A very low mosaicity is a prerequisite to apply interface-sensitive scattering techniques. The lateral domains sizes are in the range of $100\,\mu\mathrm{m}$, exhibiting a broad distribution in the total number N of the bilayers.

For measurements on samples immersed in water thick (1 cm), polished silicon blocks are used, where the neutron beam can be coupled into the substrate without refraction from the side. The beam then impinges at grazing incidence onto the sample with the incoming and reflected beam path in silicon rather than in water, avoiding incoherent scattering in H_2O or D_2O/H_2O mixtures (Fig. 22.1b). The low mosaicity of the samples prepared was preserved after immersing the samples in water.

For INS experiments highly oriented membrane stacks were prepared essentially in the same way as presented earlier [4]. However, ten or more such wafers separated by small air gaps are combined and aligned with respect to each other to create a "sandwich sample" consisting of several thousands of highly oriented lipid bilayers (total mosaicity of about 0.6°), with a total mass of several hundred milligrams of deuterated phospholipid, to maximize the scattering volume. Figure 22.1c shows a photograph of a sample for the inelastic neutron experiments.

During the neutron experiments, the solid-supported multilamellar films are kept in temperature and hydration controlled chambers. For measurements

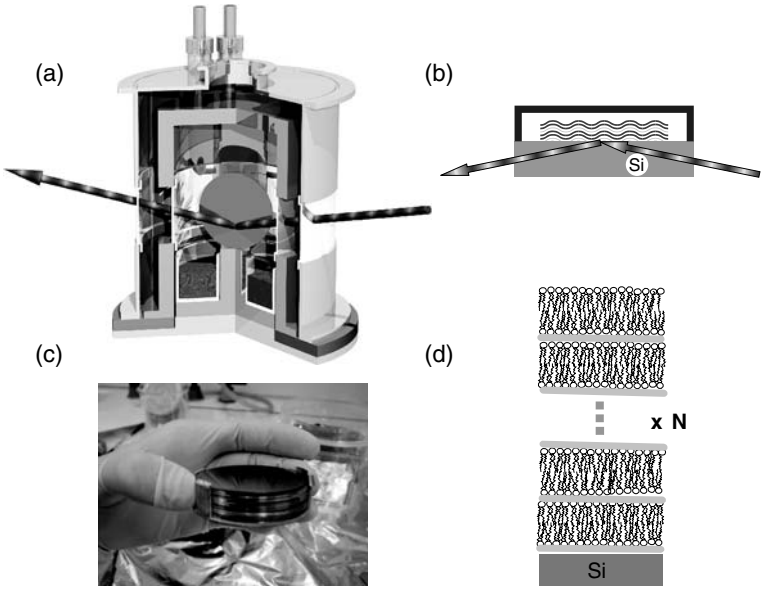

Fig. 22.1. (**a**) Schematic of the chamber used for the neutron experiments to control temperature and humidity of the bilayers. (**b**) Samples immersed in water were applied on 1 cm thick Si wafers. The neutron beam was then coupled into the wafer from the side. (**c**) Photograph of the "sandwich sample" prepared for the inelastic neutron experiments. (**d**) Hydrated multilamellar sample with layers of water (H_2O/D_2O) between the bilayers, respectively

carried out at partial hydration with the bilayers facing D_2O vapor, a chamber with two concentric high-purity aluminum cylinders was used, see Fig. 22.1a. The inner cylinder was heated or cooled by a flow of oil, connected to a temperature-controlled reservoir. The space between the two cylinders was evacuated to minimize heat conduction. The temperature was measured close to the sample holder by a Pt100 sensor, indicating a thermal stability of better than 0.02 K over several hours. At the bottom of the inner cylinder, a water reservoir was filled with salt-free Millipore water, such that the sample was effectively facing a vapor phase of nominally 100% relative humidity.

Despite the nominally full hydration condition, bilayer samples of DMPC were typically swollen only up to a repeat distance of only $d \simeq 50$–55 Å in the fluid L_α-phase, i.e., were only partially hydrated. This limited swelling of solid-supported lipid films is well known as the so-called vapor-pressure paradox, and has recently been explained by Katsaras and coworkers on the basis of small temperature gradients in the chamber [5,6]. Accordingly, it was demonstrated that chambers of suitable design do not show this effect, and that bilayers can be swollen to equilibrium (full hydration) from the vapor phase.

Alternatively, a chamber operating at full hydration has been used, where the bilayers are immersed in water, and the beam impinges through a thick

Si block as shown in Fig. 22.1b. This setup is the neutron analog of an X-ray chamber used in a recent temperature-dependent study of the specular reflectivity on aligned lipid bilayers [7]. Conditions of full hydration are important, since the diffuse (nonspecular) scattering from partially hydrated films may be affected by static defects and the associated strain fields [8], rather than by thermal diffuse scattering. Furthermore, it is desirable to probe the elasticity and fluctuation properties in the physiologically relevant state of full hydration.

22.3 Specular Neutron Reflectivity

SNR offers unique possibilities of studying the structure of thin biomolecular films and membranes on solid substrates or at the air–water interface and is widely used for this purpose complementing X-ray techniques by means of contrast variation. As is well known, the vertical structure, i.e., the laterally averaged scattering length density profile $\rho(z)$, can be derived with molecular resolution. To this end the SNR signal is measured over a large range of grazing incidence angles α_i, or vertical momentum transfer q_z. The lateral interface structure (variations of the scattering length density in the xy plane) is contained in the nonspecular scattering (NSNR) measured at angles of exit $\alpha_\mathrm{f} \neq \alpha_\mathrm{i}$ [9, 10], as discussed in Sect. 22.4

For the study of model membrane systems, an appropriate control of the sample temperature and hydration is essential. Figure. 22.2 illustrates the effect of hydration on the structure of DMPC bilayers, with two curves at partial and full hydration. Both curves correspond to the L_α phase. At full hydration the high-density (deuterated) water region becomes almost as thick as the low-density (hydrogenated) hydrophobic chain region, leading to a cancellation of

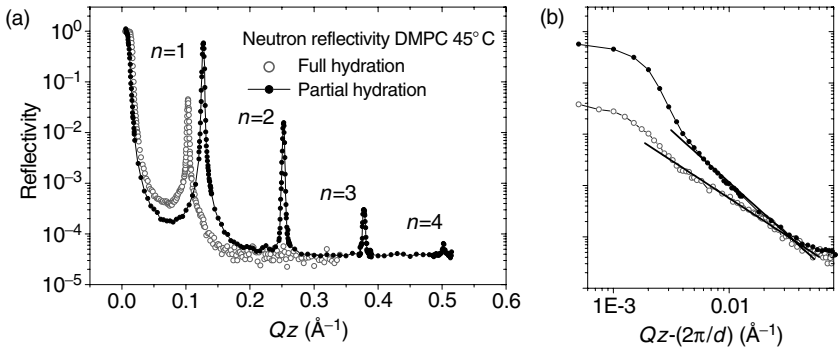

Fig. 22.2. The effect of full (*solid symbols*, measurement with sample immersed in D_2O) versus partial hydration (*open symbols*, measurement in vapor (humidity chamber)) on (**a**) the complete reflectivity curves and (**b**) of the Bragg peak tail in double logarithmic scale. Both curves correspond to DMPC in the L_α phase [4, 11]

the second-order Bragg peak. At the same time the increase in thermal fluctuations at full hydration leads to a significant damping of higher-order peak, so that only one (strong) Bragg peak is observed. At partial hydration more than four Bragg peaks can be measured, depending on the exact relative humidity (osmotic pressure).

The correct analysis of X-ray and neutron reflectivity relies on very low mosaicity (narrow orientational distribution of domains). A necessary condition is a clear distinction between specular and nonspecular scattering components. The data analysis and modeling of the measured reflectivity should be based on an appropriate scattering theory, such as the fully dynamical Parratt algorithm (taking into account multiple reflections) or on the semikinematical reflectivity pioneered by Als-Nielsen [12]. The observation of a region of total external reflection and hence of the critical angle α_c allows for the determination of the scattering length density profile on an absolute scale. Moreover, since the full q_z-range can be used for data analysis by fitting the reflectivity curve to a parametrized model of the density profile [13], a reasonable resolution in $\rho(z)$ can also be reached for fully hydrated systems. Furthermore, the phase problem is reduced, since the change of sign in the bilayer form factor (real valued due to centro-symmetry) is often accompanied by an observable cusp in the (continuously measured) reflectivity curve. Alternatively, phasing can be performed by the so-called swelling method. The advantage of full q_z-fitting has also been demonstrated in bulk (SAXS) studies, see for example [14].

In most published studies of oriented bilayers, however, only the integrated Bragg peaks of the multilamellar samples are used for data analysis, and the one-dimensional density profile $\rho(z)$ is computed by Fourier synthesis using a discrete set of Fourier coefficients f_n as described in [15, 16]. In this approach, the exact relation between Bragg peak intensity and the Fourier coefficients f_n is an open problem for which there may not even exist a general solution. Taking into account effects of absorption, polarization, specular and nonspecular Fresnel reflectivity components, illumination correction, etc., a widely used correction factor is $I_n = |f_n|^2/q_z$, where q_z^{-1} is termed a Lorentz factor for oriented bilayers. In the absence of a rigorous theoretic derivation, such a correction is at best empirical. Furthermore, the two scattering contributions of specular and nonspecular scattering are often measured in the same scan, adding up the background and making quantitative analysis questionable, since both contributions are governed by a different q_z dependence. However, the peak-to-peak distance of a reconstructed bilayer profile is luckily relatively stable against variations in data analysis like different choices of Lorentz factors.

Figure 22.3a shows DMPC reflectivity curves measured at a rather low resolution on a TAS, along with the results for the density profiles obtained by a Fourier synthesis approach (Fig. 22.3b). The data have been recorded as function of T below and above the main phase transition, simultaneously with inelastic data discussed in Sect. 22.5. The temperature-dependent structural

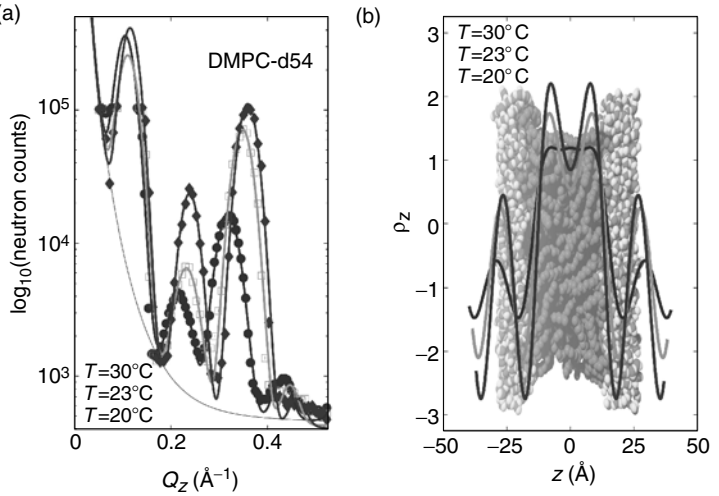

Fig. 22.3. (**a**) Reflectivity curves and (**b**) scattering length density profiles as obtained from Fourier synthesis of integrated peak intensities (d54-DMPC, hydrated from D_2O, IN12/ILL, from *top* T =30°C to *bottom* $T = 20$°C)

parameters of the bilayer profile are shown in Fig. 22.4. The two different phases show distinct differences in ρ_z. Whereas the scattering length density in the center of the bilayer in the gel phase ($T = 20$°C) is almost box shaped, it softens in the more loosely packed and dynamic fluid phase ($T = 30$°C).

The density profile $\rho(z)$ has been calculated using the relation $\rho_0(z) = \frac{2}{d_z} \sum f_n \cos\left(\frac{2n\pi}{d_z} z\right)$. Insertion of $|f_n|^2 = I_n q_z = I_n 2\pi n/d_z$ gives

$$\rho_0(z) = \frac{2}{d_z} \sum_{n=1}^{M} \sqrt{\frac{2n\pi}{d_z}} \sqrt{I_n}\, v_n \cos\left(\frac{2n\pi}{d_z}\, z\right), \quad z \in \left[-\frac{d_z}{2}, \frac{d_z}{2}\right] \tag{22.1}$$

with I_n the integrated intensity of the nth Bragg reflection, v_n the corresponding phase of f_n and d_z the periodicity of the layers in z direction. The sum goes over all orders of reflection.

In an attempt to go beyond the conventional Fourier synthesis approach, we have developed a reflectivity model in the framework of the semikinematical scattering theory, in which both the structure factor of the stack and the bilayer form factor can be suitably chosen [13], e.g., according to the given experimental resolution. This is possible since the lipid bilayer density profile $\rho_1(z)$ and the associated form factor $F(q_z)$ is parametrized by a variable number N of Fourier coefficients taken to describe the model density profile $\rho(z)$, where N is adapted to the resolution of the measurement. In contrast to conventional box models the total number of parameters can thus be kept small, while still fitting to reasonable density profiles. Moreover, structural constraints can be easily implemented by a transformation to N independent structural parameters.

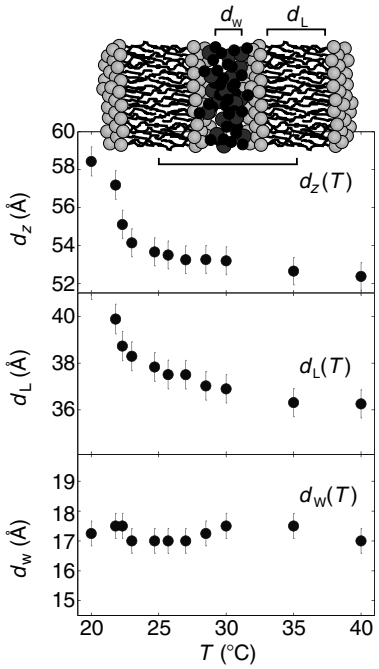

Fig. 22.4. Temperature dependence of the periodicity d_z, water layer d_w, and hydrophobic layer d_L (deuterated acyl chains) thickness of DMPC in the vicinity of the main phase transition. The values are evaluated from the density profiles as shown in Fig. 22.3

Starting point for this treatment is the so-called master equation of reflectivity from a structured interface in the semikinematic approximation [12]. There, the reflectivity from an interface with its normal along z is characterized by the (laterally averaged) scattering length density profile $\rho(z)$ (electron density profile for X-rays) between a medium 1 (air or water) with scattering length density ρ_1 and a medium 2 (solid substrate) with density ρ_2, thus

$$R(q_z) = R_F(q_z)\,|\Phi(q_z)|^2 = R_F(q_z)\,\left|\frac{1}{\Delta\rho_{12}}\int \frac{\partial\rho_e(z)}{\partial z}\mathrm{e}^{-\mathrm{i}q_z z}\mathrm{d}z\right|^2 , \qquad (22.2)$$

where R_F is the Fresnel reflectivity of the ideal (sharp) interface between the two media. $\Delta\rho_{12}$ is the scattering length density contrast. ρ is obtained by the combination of the solid surface and a step train of lipid bilayers, convolved with a function describing the positional fluctuations and multiplied by a coverage function. The critical momentum transfer or the critical angle in R_F is directly related to the density contrast by $q_z = 4\pi/\lambda\,\sin(\alpha_c) \simeq 4\sqrt{\pi\Delta\rho_{12}}$. Absorption can be accounted for by an imaginary component of the wave vector.

The solid–membrane interface is the only relevant interface for the R_F term due to the following reason: (i) in many cases the membrane sample impinges

through the water phases and there is almost no contrast between membrane and water (for X-rays), so no refraction takes place at the water–membrane interface, (ii) due to a decreasing coverage with N the water–membrane interface is much broader and less well defined, again leading to vanishing reflectivity and refraction effects at this interface. We assume a monotonously decreasing coverage function $c(N)$ with $c(1) = 1$ and $c(N) = 0$. More details of this approach are discussed in [17].

The thermal fluctuations for a solid-supported stack of lipid bilayers have been calculated in [18] and can be easily included in the structure factor, as well as a decreasing coverage function, or defect densities [19]. In practice, the range of the reflectivity determines the number N_o of orders, which should be included in the model. The parametrization of n Fourier coefficients can be easily changed by a linear transformation into a parametrization of n (independent) structural parameters of the bilayer, such as bilayer thickness (headgroup peak-to-peak), density maximum in the headgroup maximum, density in the bilayer center plane, density of the water layer, etc.

22.4 Nonspecular Neutron Reflectivity

Thermal fluctuations of lipid membranes on molecular to mesoscopic scales reflect fundamental physical properties of the lipid bilayer, related to thermodynamic stability, elasticity, interaction potentials, and phase transitions [1]. Reciprocally, fluctuations may strongly influence these phenomena, as well as different self-assembly properties of lipid membranes. If this interplay is quantitatively understood in simple model systems, more complex biomimetic membrane systems with membrane-active peptides and membrane proteins can be addressed. Thermal fluctuations in lipid bilayer phases have been probed by X-ray and neutron scattering with lineshape analysis, carried out on aqueous bulk suspensions [20,21]. Multilamellar phases of stacked lipid bilayers exhibiting smectic liquid–crystalline symmetry have received particular attention [20–23]. They allow for a tremendous increase in scattering volume over single bilayer or more dispersed phases. Interaction potentials between neighboring membranes can also be inferred from such studies [20,21,24].

However, the full information on the characteristic displacement correlation functions is lost due to powder averaging over the isotropic distribution function of domains in solution. Correspondingly, model assumptions have to be introduced in the data analysis, such as the Caillé or modified Caillé models derived from linear smectic elasticity theory. In this model two elastic constants B and K govern the compressional and bending modes of the smectic phase, respectively. For large bilayer bending rigidity $\kappa \gg kT$ typical for phospholipid systems, only the combination $\sqrt{KB}$ of the two Caillé moduli B and $K = \kappa/d$ can be inferred from the measured lineshape exponent $\eta = \pi kT/2d^2\sqrt{KB}$. The second fundamental parameter, the smectic penetration length $\Lambda = \sqrt{K/B}$ is usually not accessible, unless the bending rigidity becomes small $\kappa \simeq kT$ [20,21].

In aligned (oriented) lamellar phases on solid substrates the study of fluctuations does not suffer from the above restrictions. In such systems, specular and diffuse (nonspecular) X-ray (NSXR) and neutron reflectivity (NSNR) yield model independent information on the height–height correlation functions [8, 25]. In both cases the nonspecular (diffuse) intensity distribution can be described by a structure factor $S(q_z, q_\parallel)$, measured as a function of the parallel and vertical component of the momentum transfer [26], $q_\parallel = \sqrt{q_x^2 + q_y^2}$ and q_z, respectively.

Using NSNR in addition to NSXR or alone offers several specific advantages. The transparency of the solid substrate for neutrons gives access to a continuous range of parallel momentum transfer $q_\parallel = \sqrt{q_x^2 + q_y^2}$ at fixed vertical momentum transfer (e.g., for constant $q_z = 2\pi/d_z$), see Fig. 22.5, opening up the possibility of studying fluctuations, on length scales between a few Ångstroms up to several micrometer, essentially in one scan [4]. In time-of-flight (TOF) mode the simultaneous collection of neutrons over a

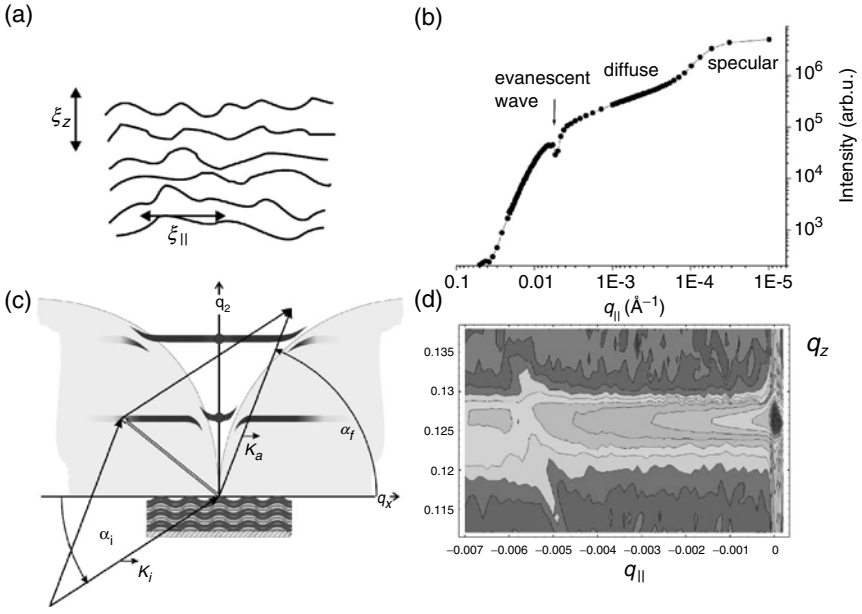

Fig. 22.5. (**a**) Schematic of fluctuating membranes causing diffuse (nonspecular) scattering. The precise nature of the height–height correlation functions, and in particular the characteristic correlation length in parallel, $\xi_\parallel$, and perpendicular direction, ξ_Z, determine the scattering distribution, as shown in (**b**) and (**d**) (DMPC, L_α phase, hydrated from D_2O [4]). (**b**) Intensity decrease with $q_\parallel$ after integration along q_z of the two-dimensional intensity mapping shown in (**d**). Refraction effects and intensity modulation due to evanescent waves are observed when the incident or exit beam is close to 0 (**c**)

range of wavelengths $\lambda \in 2, \cdots, 20\,\text{Å}$ becomes possible, significantly reducing accumulation time. Thus time-dependent white-beam measurements can be carried out without the risk of radiation damage, as is often the case in X-ray scattering. For specular reflectometry, the advantages of TOF, in particular the small accumulation times, have already been well established, e.g., see [27] and references therein. The contrast variation, which is widely used in specular neutron reflectometry [28, 29], allows to label specific molecular groups.

Up to now, only a few studies have presented quantitative analysis of nonspecular (diffuse) scattering in TOF mode, see e.g., [10, 30–32], and some technical aspects related to resolution and data treatment have to be discussed in more detail or are presently still a matter of debate.

22.4.1 Models of Bilayer Undulations

Multilamellar membrane fluctuations can be described by the linearized free energy density of a 3D smectic liquid crystal [20, 21, 33–36]. On large length scales the finite size effects and the presence of film boundaries (e.g., at the substrate) become apparent and limit the fluctuation amplitudes σ_n of the bilayers [18, 37]. On short length scales the bilayer undulations (bending and compressional modes) can be described by the bulk smectic elasticity theory using a discrete displacement field $u_n(r, z)$ for each bilayer [34–38],

$$H = \int_A \mathrm{d}^2 r \sum_{n=1}^{N-1} \left(\frac{1}{2} \frac{B}{d} (u_{n+1} - u_n)^2 + \frac{1}{2} \kappa \left(\nabla_{xy}^2 u_n \right)^2 \right) , \quad (22.3)$$

where κ denotes the bilayer bending rigidity, A the area in the xy-plane, N the number of bilayers, and u_n the deviation from the mean average position nd of the nth bilayer. B and $K = \kappa/d$ are elastic coefficients, governing the compressional and bending modes of the smectic phase, respectively. Equation 22.3 is called the discrete smectic Hamiltonian, in contrast to the continuum (Caillé) model, where the sum over n is replaced by an integral. Film boundaries can be accounted for by surface tension terms, which are not included above.

From Eq. 22.3 or similar Hamiltonians that additionally include surface terms, the characteristic height–height (displacement) correlation functions $g_{ij}(r) = \langle [u_i(\mathbf{r}') - u_j(\mathbf{r}' + \mathbf{r})]^2 \rangle$ can be calculated [18, 34, 35], describing the self and the cross-correlations of the bilayers labeled by i and j [9, 39].

The height–height self-correlation functions $g(r) = g(r, j = i)$ are a special case of particular interest. The correlation functions are characterized by several length scales: (i) the maximum lateral wavelength of fluctuations $\xi_{\max}$ (finite only in thin films, infinite in bulk systems), (ii) the rms fluctuation amplitude of the nth bilayer σ_n, measured on the lateral length scale $\xi_{\max}$, and (iii) the vertical length scale ξ_z over which the fluctuations of wavelength

$\xi_{\max}$ are correlated, defining the conformality (Fig. 22.5a). The conformality or cross-correlations of the bilayer undulations leads to the presence of diffuse Bragg sheets in reciprocal space, as can be directly verified from Eq. (22.4).

On length scales $r > \xi_{\max}$ the bilayers are essential flat, since the associated smectic damping length $\xi_z \simeq \xi_{\max}^2/\Lambda$, with $\Lambda = \sqrt{K/B}$ excludes a corresponding relaxation of the profile within the film thickness D. The presence of a sharp specular Bragg peak on top of the diffuse Bragg sheet reflects the flatness of the bilayers on the macroscopic length scale. On length scales $r \ll \xi_{\max}$ the fluctuations are not affected by the the film boundaries and should be described by bulk smectic theory. While $\xi_{\max}$ and ξ_z depend on Λ, σ scales with d^2 and the dimensionless constant $\eta = \pi kT/2d^2\sqrt{KB}$. The diffuse scattering measured in the plane of reflection can be written as a unique transformation of the $g_{ij}(r) = 2\sigma_i\sigma_j - 2c_{ij}(r)$, by [9,39]

$$S(q_x, q_z) = \frac{L_x L_y}{q_z^2} \sum_{i,j}^{N} \Delta\rho^2 \, \mathrm{e}^{-q_z^2\sigma_i\sigma_j} \, \mathrm{e}^{-\mathrm{i}q_z(h_i - h_j)} \, \epsilon_{ij}(\mathbf{q}) \tag{22.4}$$

with

$$\epsilon_{ij}(\mathbf{q}) = \int \mathrm{d}r r \left(\mathrm{e}^{q_z^2 c_{ij}(r)} - 1\right) \cos(q_x r) \; , \tag{22.5}$$

where $\Delta\rho$ is the effective scattering length contrast between the bilayer and D_2O, L_xL_y the illuminated area. The diffuse scattering is integrated over the direction perpendicular to the plane of incidence (hence over q_y), as in the present experiments. For a point-like detector slit setting, the term $\cos(q_x r)$ has to be replaced by $\mathrm{J_o}(q_\parallel r)$ with $q_\parallel^2 = q_x^2 + q_y^2$. By insertion of modeled or derived functions for $g_{ij}(r)$ in Eq. 22.4, the scattering distribution can be calculated.

In the following, we mainly consider two characteristic quantities: (i) the cross-correlation length $\xi_z(q_\parallel)$ defining the length scale over which a thermal mode is correlated as a function of the corresponding wave vector $q_\parallel$, and (ii) the decay of the q_z-integrated diffuse scattering with $q_\parallel$, i.e., the structure factor of the fluctuations. The cross-correlation function and the parameter ξ_z can be deduced from the peak lineshape and width (HWHM) along q_z. A Lorentzian lineshape indicates an exponential decrease of the cross-correlations along z with a characteristic length scale $\xi_z = 1/\mathrm{HWHM}$. Since the HWHM increases with $q_\parallel$, ξ_z depends on the wave vector of the height fluctuations, or conversely, the lateral length scale of the fluctuation. The linear smectic elasticity predicts $\xi_z = 1/(q_\parallel^2\Lambda)$.

22.4.2 Monochromatic NSNR Experiments

Using monochromatic neutrons the diffuse scattering from thermal fluctuations in phospholipid model systems has been investigated in a series of experiments as described in [4,40]. A typical mapping of the reciprocal space in

the region of the diffuse Bragg sheet is shown in Fig. 22.5d for fully hydrated DMPC in the fluid L_α phase at $T = 45°$. The modulations at values of q_x, which correspond to the transition from reflection to transmission geometry, is illustrated in Fig. 22.5c and discussed in detail in [4, 40]. With the beam near the sample horizon, the scattering is modified by refraction effects and evanescent waves. The mapping can be evaluated with respect to the self-correlation and the cross-correlation functions. Most important is the analysis of the decay of the q_z-integrated Bragg sheet intensity $\tilde{S}(q_\parallel) = \int_{\mathrm{BZ}} \mathrm{d}q_z S(q_z, q_\parallel)$, BZ denotes one Brillouin zone $2\pi/d \pm \pi/d$. It can be shown for stationary fluctuation amplitudes $\sigma_n = \text{const.}$ that the contributions of the cross-correlation terms in Eq. 22.4 vanish, and that one is left with a curve, which corresponds to the transform of an average height–height self-correlation function or the effective single-bilayer structure factor $\tilde{S}(q_\parallel)$ [41,42]. In many cases, a power law behavior is observed at high $q_\parallel$, indicating a corresponding algebraic regime of the real space correlation function at small r.

In Fig. 22.5b the integrated Bragg sheet intensity for DMPC is plotted in double logarithmic scale, illustrating the large range in intensity and parallel momentum transfer, which can be achieved in these measurements. The curve is related to the power spectral density (PSD) of the average fluctuations. In the limit of small $q_z\sigma$ the curves are strictly proportional to the SPD of the average bilayer. At finite $q_z\sigma$, the intensity decay still contains the information on the PSD, but in addition to the diffuse component there is a specular peak observed at small q_x with a Gaussian lineshape. The specular beam is clearly separated from the diffuse Bragg sheet. The systematic deviations of the observed lineshape (in particular the asymptotic power law slope) at high $q_\parallel$ from the predictions of the Caillé model have independently been found in diffuse X-ray studies of oriented bilayers, measured at full hydration, and points to the limits of the smectic model. Physical reasons for this effect are unclear. It is speculated that protrusion modes governing the fluctuations at small distances in the plane of the bilayer could explain this observation.

22.4.3 White-Beam NSNR Experiments

Neutrons in a broad range of wavelengths λ are recorded simultaneously in TOF-NSNR, and registered as a function of their respective TOF, as well as scattering angle on a two-dimensional multiwire detector. Intensity distributions can be obtained without moving any motors as a function of q_z and q_x. The TOF-NSNR data analysis includes the corrections of the raw data for detector sensitivity, wavelength distribution of the primary beam, resolution, the nontrivial transformation of the detector counts to the intensity matrix $\mathrm{I}(\theta,\lambda)$, and/or to the reciprocal space mapping to $\mathrm{I}(q_x,q_z)$ [25, 43].

Figure 22.6 shows a representative 2D data set $\mathrm{I}(2\theta, \lambda)$ of a multilamellar stack of DMPC in the fluid L_α phase at $T = 40°\mathrm{C}$. The different columns of the multiwire detector matrix correspond to different scattering angles 2θ, with

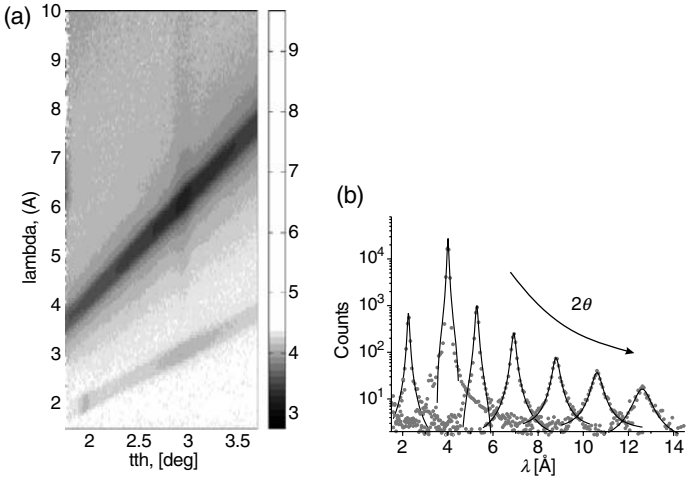

Fig. 22.6. Typical intensity distribution (logarithmically scaled gray shades) observed on the detector at D17 in TOF mode for a DMPC sample in the fluid L_α phase at T = 40°C, as a function of scattering angle 2θ (calculated from the horizontal pixel number), and neutron wavelength λ calculated from the time of flight (*left*). The angle of incidence was kept constant at $\alpha_\mathrm{i} = 2.94°$. The inclined streaks correspond to the first (*top*) and second (*bottom*) diffuse Bragg sheets. The vertical line at $2\theta = 2\alpha_\mathrm{i}$ corresponds to the specular reflectivity. Only a relatively weak specular intensity enhancement is observed over the strong diffuse signal at the Bragg peak position. The vertical cuts of the detector matrix show the intensity distribution of the first Bragg sheet as a function of λ for constant 2θ (*right*). The cuts can be fitted to a Lorentzian with HWHM values increasing with the distance away from the specular condition. The resulting HWHM values increase according to the prediction of the smectic elasticity model

$2\theta = \alpha_\mathrm{i} + \alpha_\mathrm{f}$ where α_i is the angle of incidence and α_f the exit angle. Enhanced diffuse scattering stemming from correlated thermal fluctuations is observed at the position of the diffuse Bragg sheets, for all wavelength λ and detector angles 2θ, satisfying the position of the first two diffuse Bragg sheets at $q_z = 2\pi/d$ and $q_z = 4\pi/d$ (higher-order Bragg sheets are not observed in the angular and wavelength range covered). The diffuse Bragg sheets appear as a straight line at oblique angles. The column of the matrix corresponding to $2\theta = 2\alpha_\mathrm{i}$ defines the specular axis. Its intersection with the diffuse Bragg sheets defines the specular Bragg peaks, which are enhanced over the diffuse Bragg sheets due to the specular component. From these positions, a lamellar periodicity of $d = 59$ Å is obtained. Quantitative information on the height–height correlation functions can now be obtained by evaluating the intensity matrix along the different principal axis, e.g., along the horizontal $2\theta/2$ and vertical λ axis.

As known from monochromatic X-ray and neutron scattering [44, 45], the vertical cross-correlation length $\xi_z(q_\parallel)$ of thermal fluctuations can be

inferred from the analysis of the Bragg sheet width in q_z as a function of $q_\parallel = \sqrt{q_x^2 + q_y^2}$, i.e., from the half-width at half-maximum (HWHM) $\mathrm{HWHM}_{qz}(q_\parallel)$. The conversion between HWHM_λ and HWHM_{qz} is straightforward according to $\mathrm{d}q_z/q_z = -\mathrm{d}\lambda/\lambda$. The prediction of the the smectic Hamiltonian in Eq. 22.3 is $\mathrm{HWHM}_{qz} = \Lambda q_\parallel^2$.

Cuts along λ for different constant values 2θ (Fig. 22.6) along with least-square fits to the predicted Lorentzian lineshape yield the peak width for each angle 2θ. The results can then be plotted and analyzed as a function of $\theta = 2\theta/2$ or correspondingly $q_\parallel$. The characteristic broadening with increasing θ away from the specular peak at $\theta = 2\alpha_\mathrm{i}$ is clearly observed. The curves of $\mathrm{HWHM}(q_x)$ never go to 0 for $q_x \to 0$, due to the intrinsic resolution limited width (instrument, finite size of the sample). Within the limits of resolution and experimental errors, the results of such analysis were shown to agree between monochromatic and TOF-NSNR.

Recently, the propagation of layer perturbation induced by lithographic surface gratings has been mapped by TOF-NSNR to compare thermal to static perturbations, and to have a direct control of the corresponding lateral length scales. In this case characteristic satellites occur in the diffuse Bragg sheets at the Fourier components of the surface grating [46].

22.4.4 Change of Fluctuations by Added Antimicrobial Peptides

The diffuse scattering in multilamellar systems changes upon the insertion of membrane-active molecules, such as the antibiotic peptide Magainin 2. In the system DMPC/Magainin 2 we have observed significant changes with changing the peptide-to-lipid ratio P/L, indicating corresponding changes in the fluctuation and elasticity parameters, or perhaps also the defect structure of the lamellar phase. Reciprocal space mappings $I(q_x, q_z)$ of the first Bragg sheet were measured in monochromatic mode [11] at partial hydration in the fluid L_α phase for samples of different molar ratios $P/L = 0, 0.02, 0.01, 0.033, 0.05$. Figure. 22.7 shows the reciprocal space mappings for $P/L = 0.02, 0.01$, and 0.033, from top to bottom (logarithmically scaled). The intensity of the Bragg sheet decreases with increasing P/L and the width (HWHM_{qz}) of the Bragg sheet increases with P/L. The decay of the intensities is also evident in the reflectivity curves. A corresponding disordering of the lamellar structure, possibly due to both thermal fluctuations and static defects, is observed at high P/L.

The decay of the specular Bragg peaks and the diffuse (nonspecular) Bragg sheets is accompanied by an increase in d of the lamellar stack with increasing P/L. This is probably due to electrostatic repulsion of the lamellae stemming from the increasing surface charge density, since each peptide carries about 4–5 net charges at neutral pH. It is interesting to quantify the decrease of lamellar ordering. The obvious approach would be to evaluate the parameters

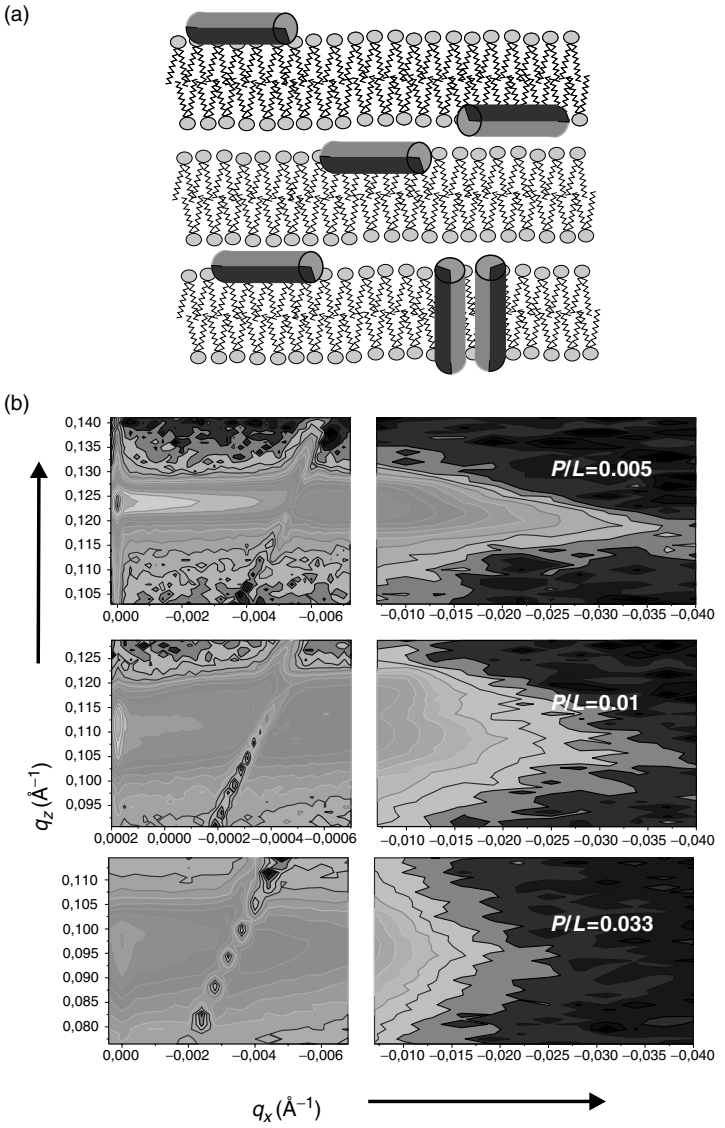

Fig. 22.7. (**a**) Schematic illustration of different states, which the peptides can adopt when bound at the bilayer. The surface (S) state versus the inserted (I) state according to the notation of Huang and coworkers, who have studied the concentration dependent transition S to I in several different amphipathic peptide systems [47–49]. (**b**) Diffuse scattering intensity in DMPC/Magainin 2 covering the relevant P/L range of the S to I transition. Reciprocal space mappings of the first Bragg sheet are shown for P/L ratios of 0.005, 0.01, and 0.033, from *top* to *bottom*. A distinct broadening of the Bragg sheet in q_z is observed, reflecting significant changes in the fluctuations spectrum with increasing peptide concentration

of the smectic model, B and Λ, as a function of P/L. However, the analysis shows that the smectic model can no longer be used to describe the data of the peptide–lipid systems. Only for $P/L = 0$, we can observe the characteristic parabolic increase in the HWHM values. For higher P/L, the width of the Bragg sheet becomes larger, but approximately constant as a function of q_x, apart from the refraction effects observed at the transition zone where α_i changes sign. An appropriate theoretic model is lacking to account for the changes in the diffuse scattering with increasing P/L, which reflect the lamellar disorder induced by the peptide, including both static defects and thermal fluctuations.

22.5 Elastic and Inelastic Studies of the Acyl Chain Correlation Peak

While the molecular structure of phospholipid model membranes has been the object of many investigations in the last three decades and is relatively well studied (see, e.g., [1]), the knowledge of membrane dynamics and in particular collective membrane dynamics, even in simple model systems as DMPC, is still scarce. Nevertheless it is now widely acknowledged that several key functions of a membrane cannot be understood without consideration of collective membrane dynamics [50]. The short wavelength dynamics is attributed to play a key role in the transport of small molecules through the membrane [51]. Molecular vibrations, conformational dynamics and "one particle" diffusion in the plane of the bilayer can be studied by a number of different spectroscopic techniques covering a range of different time scales such as incoherent inelastic and quasieleastic neutron scattering [52–54] or nuclear magnetic resonance [55]. The short-range collective motions mentioned earlier can be elucidated only by a few experimental techniques, namely coherent INS and inelastic X-ray scattering.

Figure 22.8 shows examples of some of the motions that can be probed by coherent neutron scattering, as there are bilayer undulation modes with typical length scales of several hundred Ångströms and short wavelength density fluctuations on nearest neighbor distances of the hydrocarbon acyl chains in the plane of the bilayer, which we discuss in the following. Recently Chen et al. made a seminal inelastic measurements in phosphocholine model membranes using IXS techniques [56]. They could determine the dispersion relation in the gel and the fluid phase of DLPC bilayers, finding a minimum at Q_0, the maximum of the static structure factor $S(Q)$.

22.5.1 Inelastic Neutron Scattering

We applied INS for the study of the collective dynamics of the hydrocarbon acyl chains in lipid bilayers [57]. The main differences with respect to inelastic

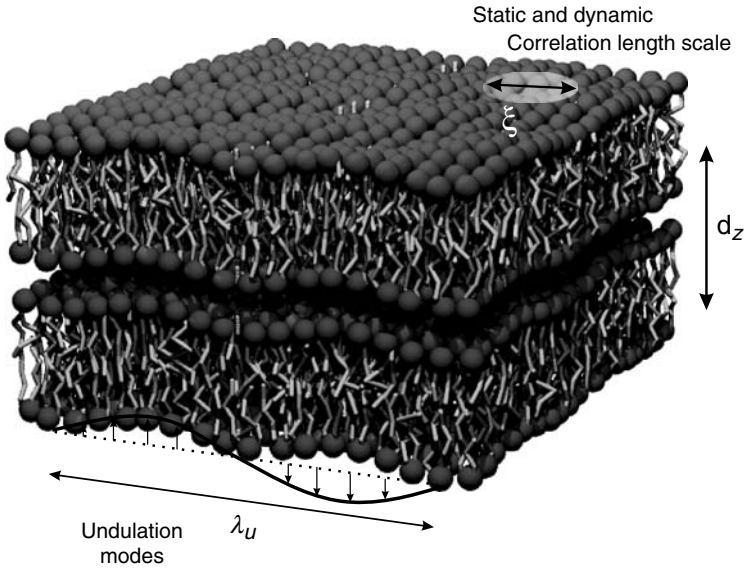

Fig. 22.8. Schematic of a double bilayer with some elementary excitations and the corresponding length scales. Apart from undulation modes with typical wavelengths of several hundred Ångströms, the short wavelength correlations and dynamics in the plane of the membrane can be probed by coherent neutron scattering. The corresponding length scale ξ is thereby in the order of 20 Å. d_z is the bilayer thickness

X-ray scattering are related to the energy–momentum relation of the neutron versus the photon probe, strongly affecting energy resolution, and accessible (Q,ω) range. At high Q the energy of the incident neutrons is in the range of the excitations (some microelectron volts) resulting in a high energy resolution (up to $\sim$300 μeV), in comparison to 1.5 meV of the inelastic X-ray experiment. A better energy resolution in combination with a smaller ratio between central peak and Brillouin amplitudes leads to very pronounced satellites, which are easier to evaluate. This is of particular advantage for the identification of peaks in the central part of the dispersion relation, as well as for the experimental verification of a predicted nondispersive mode at high energies, as shown later. Due to the dispersion relation of the neutron itself ($\sim Q^2$), the range at low Q and high ω values is difficult to access by INS. The determination of the exact speed of sound is therefore a domain of inelastic X-ray scattering.

The collective dynamics of the lipid acyl chains in the model system DMPC (-d54, deuterated 1,2-dimyristoyl-*sn*-glycero-3-phosphatidylcholine), were studied by INS. By selective deuteration of the chains, the respective motions are strongly enhanced over other contributions to the inelastic scattering

cross-section. The dynamical structure factor $S(Q_r, \omega)$ in the gel (P_β) and fluid (L_α) phase, and its temperature dependence in the vicinity of the main phase transition has been investigated. The measurements were carried out on the cold TAS IN12 and the thermal spectrometer IN3 at the high flux reactor of the ILL in Grenoble, France, the principles of which are described next.

The concept of TAS has undoubtedly been very successful in the investigation of collective excitations in condensed matter physics, i.e., phonons and magnons in crystals. Advantages of TAS are their relatively simple design and operation and the efficient use of the incoming neutron flux to the examination of particular points in (Q, ω) space. Figure 22.9 shows a schematic of a TAS. By varying the three axes of the instrument, the axes of rotation of the monochromator, the sample and the analyzer, the wavevectors $\boldsymbol{k}_\mathrm{i}$ and $\boldsymbol{k}_\mathrm{f}$

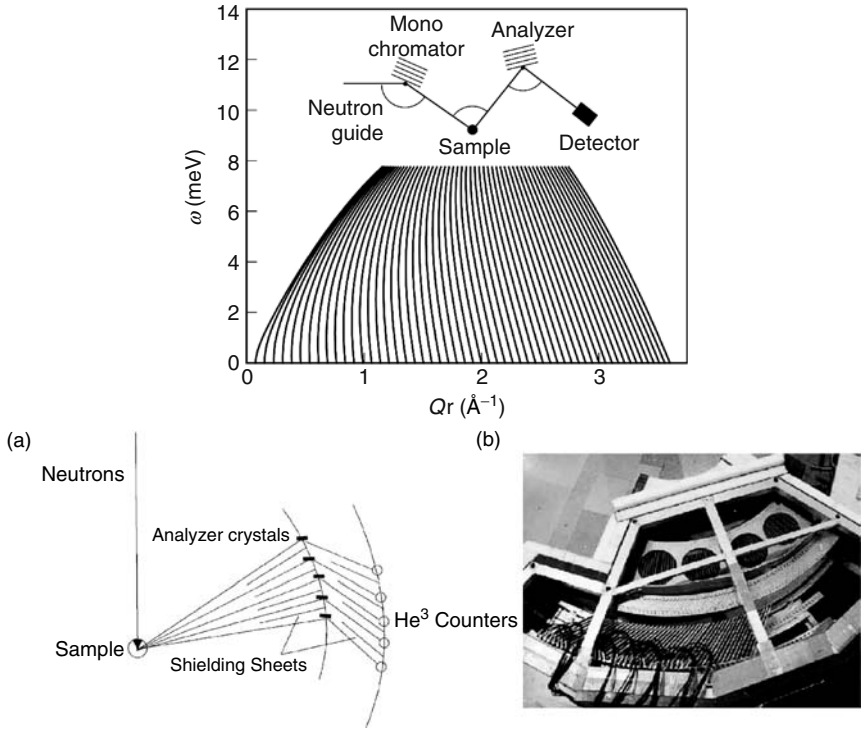

Fig. 22.9. Accessible (Q,ω) range of the cold TAS IN12 (*top*). The inset shows a schematic of a triple-axis instrument with monochromator, sample and analyzer. Principle of IN3's multianalyzer detector (*bottom* (**a**)). 32 Cu-analyzer blades with a dedicated ^{3}He counter (from [59]) each covering 1° in scattering angle 2θ (**b**). All analyzers are arranged on a circle (with a radius of 1031 mm) and aligned to the same final energy of $E_\mathrm{f} = 31$ meV

and the energies E_i and E_f of the incident and the scattered beam, respectively, can be determined. $\mathbf{Q}$, the momentum transfer to the sample, and the energy transfer, ω, are then defined by the laws of momentum and energy conservation:

$$\mathbf{Q} = \boldsymbol{k}_\mathrm{f} - \boldsymbol{k}_\mathrm{i} \quad \text{and} \quad \omega = E_\mathrm{i} - E_\mathrm{f}. \tag{22.6}$$

The accessible ($\mathbf{Q}$,ω) range of IN12 for a fixed energy of the scattered beam E_f of 10 meV is shown in Fig. 22.9 and covers very well the range of the excitations expected in phospholipid model membranes. It is limited by the range of incident neutron energies offered by the neutron guide as well as by mechanical restrictions of the spectrometer. The instrumental energy resolution in this configuration is $\Delta\omega = 500\,\mu\mathrm{eV}$. By choosing smaller incident energies and energy transfers the energy resolution can be enhanced. A detailed description of the experimental set-up and method can be found elsewhere [57, 58].

With a conventional TAS, single points in (Q,ω) space are scanned one by one. A more efficient use of the triple-axis technique is achieved by *multiplexing*, i.e., the use of several independent analyzer blades and position-sensitive detectors to investigate multiple (Q,ω) points at the same time. This option is implemented on the spectrometer IN3 by the usage of a multianalyzer detector. A schematic of the set-up is shown in Fig. 22.9a; Fig. 22.9b shows a photograph of the detector unit with analyzers and ^{3}He counter tubes (for a detailed description of the set-up see Demmel et al., [59]).

The use of the multidetector is especially useful in systems with restricted dimensions. Considering the membranes as stacked two-dimensional layers, only two directions in space can be differentiated, i.e., the plane of the bilayer, Q_r, or the normal to it, Q_z. Because of the missing periodicity in the third direction in space the scattered intensity is distributed rod-like in reciprocal space. The scattering is independent of one of the reciprocal axis and this allows to measure different $\mathbf{Q}$ vectors of the sensitive reciprocal axis at the same time in the different channels of the multi analyzer. The dispersion relation can therewith be measured for several Q-points at the same time. Considering elastic scattering, large areas of reciprocal space can be measured (or *mapped*) simultaneously.

22.5.2 Elastic Neutron Scattering

The use of a TAS offers the possibility of measuring the static structure factor in the plane of the membranes, $S(Q_r)$, the in-plane dynamics, $S(\mathrm{Q}_r, \omega)$, and the reflectivity on the same instrument in the same run without changing the setup (diffraction is measured at energy transfer $\omega = 0$). This is an invaluable advantage as the thermodynamic state of the lipid bilayer not only depends on temperature and relative humidity, but also on cooling and heating rates, preparation and thermal history. The combination of elastic and inelastic measurements (see later) leads to a complete picture of structure and (collective) dynamics of model membranes on a molecular length scale.

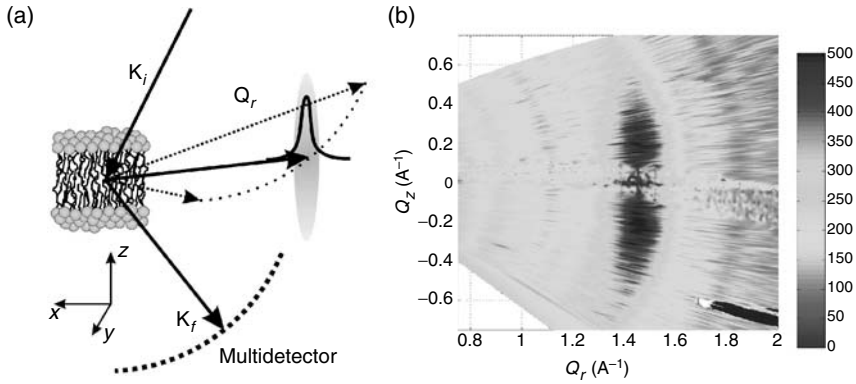

Fig. 22.10. (**a**) A typical multidetector Q-scan in reciprocal space. The incident (k_i) and the outgoing beam (k_f) and the resulting momentum transfers Q for the different analyzer blades are given in the figure. (**b**) By rotating (rocking) the sample, the reciprocal (Q_r, Q_z) space around the chain correlation peak can be mapped. The measurement was done in the gel phase of the phospholipid bilayer at $T = 20^\circ$

Figure 22.10 shows a (Q_r,Q_z) mapping of the interacyl chain correlation peak in the gel phase of the deuterated DMPC bilayer at $T = 20°$C. Because of the quasi two dimensionality of the system, the peak is sharp in Q_r, but the intensity is smeared out in the perpendicular Q_z-direction. The data show excellent agreement with results of molecular dynamics (MD) simulations on the structure of lipid bilayers [60].

On IN12 temperature-dependent Q-scans through the interacyl chain peak of deuterated DMPC in the temperature range from $T = 20°$C to $T = 40°$C were performed to probe the static correlations in the plane of the bilayer. Figure 22.11a shows Q-scans of the interchain correlation peak at temperatures of $T = 20$, $T = 23$, and $T = 30°$C, respectively. The deuterated compound undergoes the phase transition from the more rigid gel phase into the liquid-like fluid phase at about T_c=21°C, some degrees lower than in the protonated compound. When going from the gel to the fluid phase, the peak position changes to smaller Q_r-values (larger average nearest neighbor distances) and the peaks broaden, indicating a decreasing correlation length ξ_r in the plane of the membranes.

Figure 22.11b gives Q_0, the amplitude I and the correlation length ξ_r as obtained from the peak position, amplitude and width of the peak for all measured temperatures from $T = 20$–40°C. The average nearest neighbor distance, as calculated from $2\pi/Q_0$, enlarges with temperature. Although the phase transition is of first order [22, 23, 61], the values point to a critical behavior (anomalous swelling) of the bilayer. As the analyzer cuts out only the elastically scattered neutrons and the quasielastic contribution to the background is reduced, the signal-to-noise ratio is drastically improved.

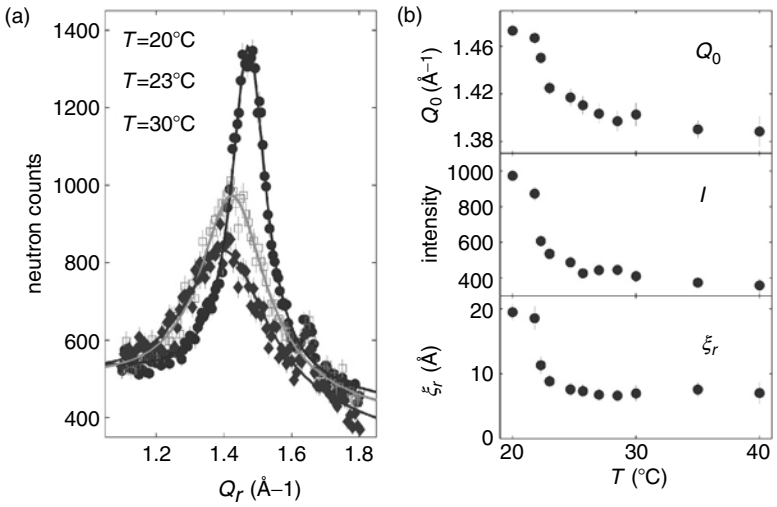

Fig. 22.11. (**a**) Q-scans of the acyl chain peak for temperatures from *top* to *bottom* $T = 20$, $T = 23$, and $T = 30°$C through the main phase transition of the DMPC-d54 bilayer. (**b**) Q_0, intensity and correlation length ξ_r as extracted from peak position, amplitude and width for all measured temperatures between $T = 20$ and $40°$

22.5.3 Collective Dynamics

A typical energy scan of deuterated DMPC collected at $T = 20°$C, in the gel phase of the bilayer, measured on IN12 at $Q = 1.0\,\text{Å}^{-1}$ is shown in Fig. 22.12. The inset shows the excitations of the bilayer in the gel and the fluid phase ($T = 30°$C, nine degrees above the phase transition temperature), exhibiting well-pronounced peaks the position and width of which can be easily determined. The inelastic scans can be evaluated by the generalized three-effective eigenmode theory (GTEE) [56, 62, 63], using the following function for least-square fitting:

$$\frac{S(Q,\omega)}{S(Q)} = \frac{1}{\pi}\left(A_0\frac{\Gamma_h}{\omega^2+\Gamma_h^2} + A_s\left[\frac{\gamma_s + b(\omega+\omega_s)}{(\omega+\omega_s)^2+\gamma_s^2} + \frac{\gamma_s - b(\omega-\omega_s)}{(\omega-\omega_s)^2+\gamma_s^2}\right]\right).$$

The model consists of a heat mode, centered at $\omega = 0\,$meV (Lorentzian with a width Γ_h), two sound modes, represented by Lorentzians at $\omega = \pm\omega_s$ and a damping γ_s [62, 63]. From the width of the central mode, and the width and position of the Brillouin lines, the thermal diffusivity, the sound frequency, and the sound damping can be determined, respectively, within the framework of a hydrodynamic theory. To fit the neutron data an additional Lorentzian component is added describing the broad quasielastic contribution presumably

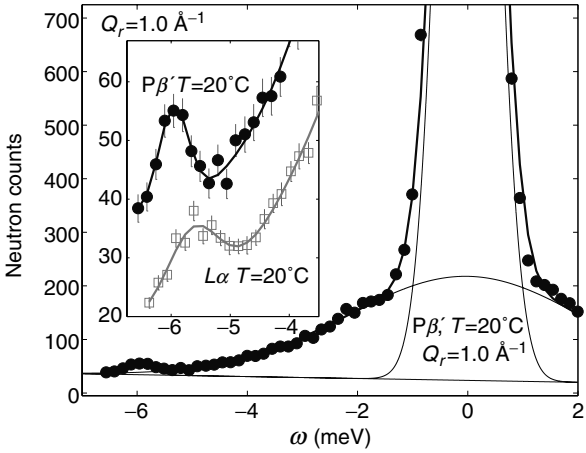

Fig. 22.12. Energy scan at a $Q_r = 1.0\,\text{Å}^{-1}$ in the gel phase of the bilayer. The inset shows the excitations of the bilayer in the gel (*top*) and the fluid phase (*bottom*)

associated with intramolecular degrees of freedom and incoherent scattering, not seen by inelastic X-ray scattering. The solid line in Fig. 22.12 is a fit by the three-effective eigenmode model with an additional Lorentzian component.

Figure 22.13a shows the dispersion relation in the gel and the fluid phase as measured by several constant Q-scans at Q-values ranging from $Q = 0.7$ to $3.0\,\text{Å}^{-1}$. The fluid dispersion has been measured far in the fluid phase of the DMPC bilayer. At small Q_r, longitudinal sound waves in the plane of the bilayer are probed and give rise to a linear increase of $\omega \propto Q_r$, saturating at some maximum value ("maxon"), before a pronounced minimum Ω_0 ("roton") is observed at $Q_0 \simeq 1.4\,\text{Å}^{-1}$, the first maximum in the static structure factor $S(Q_r)$ (the interchain correlation peak). Qualitatively, this can be understood if Q_0 is interpreted as the quasi-Brillouin zone of a two-dimensional liquid. Collective modes with a wavelength of the average nearest neighbor distance $2\pi/\mathrm{Q}_0$ are energetically favorable, leading to the found minimum. At Q_r values well above the minimum, the dispersion relation is dominated by single particle behavior. The inelastic neutron data are less noisy and cover a wider range as compared to inelastic X-ray scattering [56]. A quantitative theory that predicts the absolute energy values of "maxon" and "roton" on the basis of molecular parameters is absent so far. However, the dispersion relation can be extracted from MD simulations by temporal and spatial Fourier transformation of the molecular real space coordinates [64] which shows excellent agreement.

Figure 22.13b shows corresponding energy scans taken at $Q = 1.5\,\text{Å}^{-1}$ in the dispersion minimum for temperatures T between 20 and 40°C. In the gel phase an excitation at $\omega_s = -1\,\text{meV}$ is found. At higher temperatures, the gel excitations decreases and a new excitation at energy values of $\omega_s = -2\,\text{meV}$ grows associated with the fluid phase. Clearly the excitations are not spurious

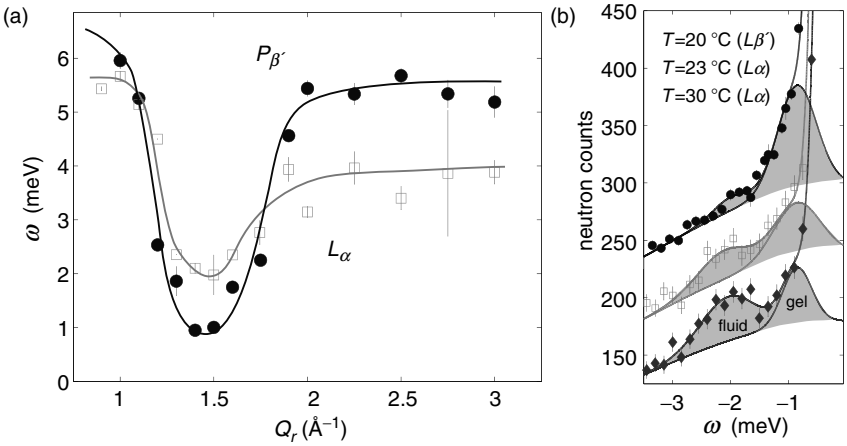

Fig. 22.13. (**a**) Dispersion relations in the gel and the fluid phase of the DMPC bilayer as measured by several constant Q-scans at Q values ranging from Q=0.7 to 3.0 Å^{-1}. (**b**) Energy scans in the dispersion minimum at $Q = 1.5$ Å^{-1} for temperatures $T = 20°$C, $T = 23°$C, and $T = 30°$C (from *top* to *bottom*)

effects as they are symmetric around the central peak. The assignment of the excitations to the particular phases is justified by their temperature dependence as in each phase there is a dominant excitation. Both modes are clearly dispersive and change its energy position when moving out of the minimum (Fig. 22.13a). Small traces of the "fluid excitation" are already present in the gel phase. At $T = 30°$C, far in the fluid phase, the "gel excitation" is still present, indicating coexistence of fluid-phase and gel-phase domains. This coexistence is only observed in the range of the dispersion minimum, which coincides with the maximum of the static structure factor. One has to note that at the same time, the elastic scans do not show coexistence of two phases. While the transition is of first order, a pseudocritical swelling, i.e., a continuous change of the interlamellar distance in the range of T_c, is observed for DMPC and other lipids [22, 61, 65]. The changes in d_z (see Fig. 22.3) are accompanied by corresponding changes in the mean distance between the acyl chains (Fig. 22.11b).

A crucial point is the size of the domains. The coexistence of macroscopic domains with sizes larger than the coherence length ξ_n of the neutrons in the sample would lead to a peak splitting of the acyl chain peak. Therefore, the domain sizes must be smaller than a few hundred angstroms estimated for ξ_n. Fluid domains in the gel phase and vice versa with sizes smaller than 0.01 µm^2 have been reported in a recent AFM study [66], and have been related to lateral strain resulting from density differences in both phases. While the "maxon" and the high-Q range are energetically higher in the gel than in the fluid phase (due to stiffer coupling between the lipid

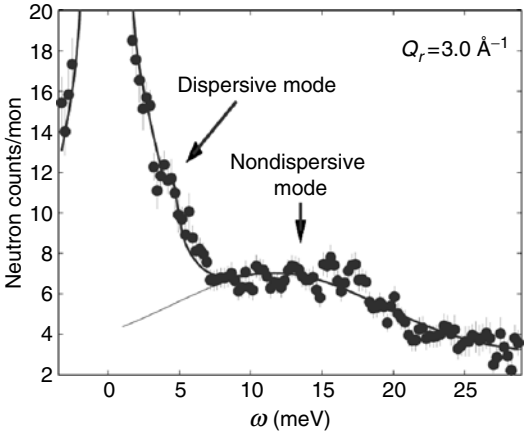

Fig. 22.14. Scan over a higher energy transfer range at Q_r=3.0 Å^{-1} (IN3 data), showing both the dispersive excitation and the nondispersive (optical) excitation predicted by MD calculation

chains in all-*trans* configuration), Ω_0, the energy value in the dispersion minimum, is actually smaller in the gel phase, roughly analogous to soft modes in crystals.

Figure 22.14 shows an energy scan in the gel phase at Q_r=3.0 Å^{-1}, up to an energy transfer of 30 meV. Aside from the dispersive excitation due to in-plane density waves, a second nondispersive (optical) mode is observed at about $\omega = 14$ meV with a width (FWHM) of about 13 meV, corresponding quite well to the predictions by Tarek et al., [64], and can be attributed to the motions of the methyl ends of the acyl chains. This mode was not observed by Chen et al., possibly due to the low signal-to-noise ratio in the inelastic X-ray measurements at high energy transfers.

22.6 Conclusions

Only a few methods are currently available to determine the fundamental smectic length scale Λ or the bilayer bending rigidity κ. While light scattering or optical microscopy techniques determine κ from thermal fluctuations on much larger length scales, which may lead to different values, X-ray powder diffraction and line shape analysis is sensitive to Λ only in the limit of very soft and strongly undulating systems, untypical for phospholipids. By nonspecular neutron and X-ray scattering from aligned phases the bilayer structure and fluctuation is accessible over a wide range both for relatively stiff and soft systems, covering length scales from the molecular scale up to a few 100 nm.

Nonspecular neutron scattering is a very useful tool to elucidate phospholipid membrane interaction on the basis of changing fluctuation and elasticity properties as described in this chapter. To this end, an appropriate model is

needed. Turner and Sens have explored the statistical physics of particle inclusions in smectic liquid crystals [67,68], providing a quantitative description of the deformation fields around static defects, as caused by inclusions. Their model, however, is based on the smectic model, and the inclusions lead to effective smectic parameters, while the present data show that the scattering distribution can no longer be described by Caillé theory.

Furthermore, the following problems are associated with the verification of the parabolic law $\mathrm{HWHM}_{qz}(q_x)$ predicted for smectic systems: (i) the width saturates for $q_x \geq 0.01\,\text{Å}^{-1}$, indicating contributions from collective molecular motions that are distinct from bending, (ii) the initial increase in the curve shows some spread and may also be explained by functions other than parabolas. The first point is accompanied by corresponding deviations from the smectic model in the curve $S(q_x)$ also observed at high q_x. We speculate that collective protrusion of peristaltic modes of the bilayers is at the origin of this observation. The present results have been verified by different samples and show consistency between two completely different modes of the experiments, monochromatic and TOF. However, suitable techniques of measuring the resolution, i.e., the intrinsic width of the cross-sections (cuts) along λ for constant angles 2θ have to be developed, in order to verify the resolution model according to [43].

Measurements of the collective short wavelength dynamics in lipid bilayers are a new but promising field, because the collective dynamics is likely to play a crucial role for different biological functions. The use of a triple-axis spectrometer allows to measure structure and dynamics, i.e., reflectivity, acyl chain correlation peak and in-plane dynamics, of model membranes on a molecular length scale in the same run without changing set-up. The dispersion relation measured in the gel and the fluid phase of the DMPC model system and the interpretation of the temperature dependent experiments point to a new interpretation of the gel–fluid phase transition and the collective excitations in lipid bilayers. Further inelastic investigations will address the influence of different head and tail groups to the collective dynamics.

On the interaction of peptides with model membranes the results presented also show that pronounced changes of the fluctuation spectrum occur already at moderate peptide concentration, e.g., at $P/L = 0.005$, where the changes in the specular reflectivity are still quite small. Furthermore the influence of cholesterol and membrane-active proteins will be studied, hopefully giving new insight into the functionality of these systems. The investigation of more and more complex systems might once lead to a better understanding of real biological membranes.

Acknowledgments

We thank R. Cubitt for helpful comments and for his great achievements in the design and construction of the novel D17 reflectometer, C. Münster and

C. Ollinger for enjoyable collaborations on some of the original work discussed here, R. Siebrecht and V. Leiner for excellent support at ADAM, F. Demmel for help on the IN3 multidetector, G. Fragneto for experimental support and discussions and G. Brotons for helpful discussions regarding the data analysis. Financial aid by the Deutsche Forschungsgemeinschaft (DFG) through grants SA-772/3 and SA-772/4 and by the German Research Ministry under contract numbers 05300CJB6 and 05KS1TSA7 is gratefully acknowledged.

References

1. R. Lipowsky, E. Sackmann (eds.), *Structure and Dynamics of Membranes*, Vol. 1, *Handbook of Biological Physics* (Elsevier, North-Holland, Amsterdam, 1995)
2. G. Büldt, H.U. Gally, J. Seelig, G. Zaccai, J. Mol. Biol. **135** (1979), 673
3. M. Seul, M.J. Sammon, Thin Solid Films **185** (1990), 287
4. C.M. Münster, T. Salditt, M. Vogel, R. Siebrecht, J. Peisl, Europhys. Lett. **46** (1999), 486
5. J. Katsaras, Biophys. J. **75** (1998), 2157
6. J.F. Nagle, J. Katsaras, Phys. Rev. E **59** (1999), 7018
7. M. Vogel, C. Münster, W. Fenzl, T. Salditt, Phys. Rev. Lett. **84** (2000), 390
8. T. Salditt, C. Münster, J. Lu, M. Vogel, W. Fenzl, A. Souvorov, Phys. Rev. E **60** (1999), 7285
9. S.K. Sinha, E.B. Sirota, S. Garoff, H.B. Stanley, Phys. Rev. B **38** (1988), 2297
10. R. Pynn, Phys. Rev. B **45** (1992), 602
11. C. Münster, PhD thesis, Sektion Physik, Universität München, 2000
12. J. Als-Nielsen, D. McMorrow, *Elements of Modern X-Ray Physics* (John Wiley & Sons, New York, 2001)
13. T. Salditt, C. Li, A. Spaar, U. Mennicke, Eur. Phys. J. E **7** (2002), 105
14. G. Pabst, M. Rappolt, H. Amenitsch, P. Laggner, Phys. Rev. E **62** (2000), 4000
15. A.E. Blaurock, Biochem. Biophys. Acta **650** (1982), 167
16. J. Katsaras, Biochem. Cell. Biol. **73** (1995), 209
17. T. Salditt, Curr. Opin. Coll. Interface Sci. **19** (2000), 232
18. D. Constantin, U. Mennicke, C. Li, T. Salditt, Eur. Phys. J. E **12** (2003), 283
19. U. Mennicke, PhD thesis, Institut für Röntgenphysik, Georg-August-Universität Göttingen, 2003
20. C.R. Safinya, E.B. Sirota, D. Roux, G.S. Smith, Phys. Rev. Lett. **57** (1986), 2718
21. C.R. Safinya, E.B. Sirota, D. Roux, G.S. Smith, Phys. Rev. Lett., **62** (1989), 1134
22. J.F. Nagle, H.I. Petrache, N. Gouliaev, S. Tristram-Nagle, Y. Liu, R.M. Suter, K. Gawrisch, Phys. Rev. E, **58** (1998), 7769
23. H.I. Petrache et al., Phys. Rev. E **57** (1998), 7014
24. R.P. Rand, V.A. Parsegian, Biochim. Biophys. Acta **988** (1989), 351
25. T. Salditt, C. Münster, U. Mennicke, C. Ollinger, G. Fragneto, Langmuir **19** (2003), 7703
26. G. Smith, E.B. Sirota, C.R. Safinya, N.A. Clark, Phys. Rev. Lett. **60** (1988), 813
27. R.K. Thomas, J. Penfold, Curr. Opin. Coll. Interface Sci. **1** (1995), 23
28. T.M. Bayerl, R.K. Thomas, A. Rennie, J. Penfold, E. Sackmann, Biophys. J. **60** (1991), 1

29. T.L. Kuhl, J. Majewski, J.Y. Wong, S. Steinberg, D.E. Leckband, J.N. Israelachvili, G.S. Smith, Biophys. J. **75** (1998), 2352
30. G.P. Felcher, R.J. Goyette, S. Anastasiadis, T.P. Russell, M. Foster, F. Bates, Phys. Rev. B **50** (1994), 9565
31. S. Langridge, J. Schmalian, C.H. Marrows, D.T. Dekadjevi, B.J. Hickey, Phys. Rev. Lett. **85** (2000), 4964
32. Z.X. Li, J.R. Lu, R.K. Thomas, A. Weller, J. Penfold, J.R.P. Webster, D.S. Sivia, A.R. Rennie, Langmuir **17** (2001), 5858
33. W. Helfrich, Z. Naturforsch. **28c** (1973), 693
34. L. Ning, C.R. Safinya, R. Bruinsma, J. Phys. II France **5** (1995), 1155
35. N. Lei, PhD thesis, Rutgers, 1993
36. A. Caillé, C. R. Acad. Sci. **274** (1971), 891
37. R. Holyst, D.J. Tweet, L.B. Sorensen, Phys. Rev. Lett. **65** (1990), 2153
38. J. Als-Nielsen, J.D. Litster, R.J. Birgenau, M. Kaplan, C.R. Safinya, Phys. Rev. B **22** (1980), 312
39. S.K. Sinha, J. Phys. III (France) **4** (1994), 1543
40. A. Schreyer, R. Siebrecht, U. Englisch, U. Pietsch, H. Zabel, Physica B **248** (1998), 349
41. T. Salditt, T.H. Metzger, J. Peisl, Phys. Rev. Lett. **73** (1994), 2228
42. T. Salditt, D. Lott, T.H. Metzger, J. Peisl, G. Vignaud, P. Høghøj, O. Schärpf, P. Hinze, R. Lauer, Phys. Rev. B **54** (1996), 5860
43. R. Cubitt, G. Fragneto, Appl. Phys. A **74** (2003), 329
44. M. Vogel, PhD thesis, Universität Potsdam, 2000
45. T. Salditt, M. Vogel, W. Fenzl, Phys. Rev. Lett. **90** (2003), 178101
46. C. Ollinger, D. Constantin, J. Seeger, T. Salditt, Europhys Lett. **71** (2005), 311
47. S. Ludtke, K. He, H. Huang, Biochemistry, **34** (1995), 16764
48. S.J. Ludtke, K. He, W.T. Heller, T.A. Harroun, L. Yang, H.W. Huang, Biochemistry **35** (1996), 13723
49. L. Yang, T.M. Weiss, R.I. Lehrer, H.W. Huang, Biophys. J. **79** (2000), 2002
50. T. Bayerl, Curr. Opin. Coll. Interface Sci. **5** (2000), 232
51. S. Paula, A.G. Volkov, A.N. Van Hoek, T.H. Haines, D.W. Deamer, Biophys. J. **70** (1996), 339
52. W. Pfeiffer, Th. Henkel, E. Sackmann, W. Knorr, Europhys. Lett. **8** (1989), 201
53. S. König, T.M. Bayerl, G. Coddens, D. Richter, E. Sackmann, Biophys. J. **68** (1995), 1871
54. E. Endress, H. Heller, H. Casalta, M.F. Brown, T.M. Bayerl, Biochemistry **41** (2002), 13078
55. A.A. Nevzorov, M.F. Brown, J. Chem. Phys. **107** (1997), 10288
56. S.H. Chen, C.Y. Liao, H.W. Huang, T.M. Weiss, M.C. Bellisent-Funel, F. Sette, Phys. Rev. Lett. **86** (2001), 740
57. M.C. Rheinstädter, C. Ollinger, G. Fragneto, F. Demmel, T. Salditt, Phys. Rev. Lett. **93** (2004), 108107
58. M.C. Rheinstädter, C. Ollinger, G. Fragneto, T. Salditt, Physica B **350** (2004), 136
59. F. Demmel, A. Fleischmann, W. Gläser, Nucl. Instrum. Methods Phys. Res., Sect. A **416** (1998), 115
60. A. Spaar, T. Salditt, Biophys. J. **85** (2003), 1576
61. F.Y. Chen, W.C. Hung, H.W. Huang, Phys. Rev. Lett. **79** (1997), 4026
62. C.Y. Liao, S.H. Chen, F. Sette, Phys. Rev. Lett. **86** (2001), 740
63. T.M. Weiss, P.-J. Chen, H. Sinn, E.E. Alp, S.H. Chen, H.W. Huang, Biophys. J. **84** (2003), 3767

64. M. Tarek, D.J. Tobias, S.-H. Chen, M.L Klein, Phys. Rev. Lett. **87** (2001), 238101
65. P.C. Mason, J.F. Nagle, R.M. Epand, J. Katsaras, Phys. Rev. E **63** (2001), 030902(R)
66. A.F. Xie, R. Yamada, A.A. Gewirth, S. Granick, Phys. Rev. Lett. **89** (2002), 246103
67. P. Sens, M.S. Turner, J. Phys II. France **7** (1997), 1855
68. P. Sens, M.S. Turner, Phys. Rev. E **55** (1997), R1275